Supporting Information

Optoelectronic manifestation of orbital angular momentum driven by chiral hopping in helical Se chains

Bumseop Kim[1,2†], Dongbin Shin[3,4†], Seon Namgung[2], Noejung Park[1,2], Kyoung-Whan Kim[5*], Jeongwoo Kim[6*]

[1]*Graduate School of Semiconductor Materials and Devices Engineering, Ulsan National Institute of Science and Technology, Ulsan 44919, Korea*

[2]*Department of Physics, Ulsan National Institute of Science and Technology, Ulsan 44919, Korea*

[3]*Department of Physics and Photon Science, Gwangju Institute of Science and Technology, Gwangju 61005, Korea*

[4]*Max Planck Institute for the Structure and Dynamics of Matter and Center for Free Electron Laser Science, Hamburg 22761, Germany*

[5]*Center for Spintronics, Korea Institute of Science and Technology, Seoul 02792, Korea*

[6]*Department of Physics, Incheon National University, Incheon 22012, Korea*

[†]These authors contributed equally: Bumseop Kim, Dongbin Shin

*corresponding author e-mail

kwk@kist.re.kr; kjwlou@inu.ac.kr

Note S1. Diagonalization of the model Hamiltonian for a one-dimensional chiral Se chain.

Here we diagonalize the 9 × 9 matrix

$$H = \begin{pmatrix} h_{\mathrm{on}} & h_{\mathrm{hop}} & h_{\mathrm{hop}}^{\dagger} \\ h_{\mathrm{hop}}^{\dagger} & h_{\mathrm{on}} & h_{\mathrm{hop}} \\ h_{\mathrm{hop}} & h_{\mathrm{hop}}^{\dagger} & h_{\mathrm{on}} \end{pmatrix}, \tag{S1}$$

in the $|A\rangle,|B\rangle,|C\rangle$ atomic basis. Here h_{on} and h_{hop} are given by the following 3 × 3 matrices, respectively.

$$h_{\mathrm{on}} = \begin{pmatrix} \epsilon_r & 0 & 0 \\ 0 & \epsilon_t & 0 \\ 0 & 0 & \epsilon_z \end{pmatrix}, h_{\mathrm{hop}} = e^{ik_z a} \begin{pmatrix} t_{rr} & -t_{tr} & -t_{zr} \\ t_{tr} & t_{tt} & t_{zt} \\ t_{zr} & t_{zt} & t_{zz} \end{pmatrix}, \tag{S2}$$

in the $|p_r\rangle,|p_t\rangle,|p_z\rangle$ orbital basis. We first diagonalize the atomic degree of freedom. One can show that equation (S1) is diagonalized by the following eigenstates.

$$|\mu\rangle = \frac{1}{\sqrt{3}}\left(e^{-2\pi i\mu/3}|A\rangle + |B\rangle + e^{2\pi i\mu/3}|C\rangle\right), \tag{S3}$$

where $\mu = -1,0,1$. The corresponding eigen-Hamiltonians are given by

$$h_{\mathrm{on}} + 2\mathrm{Re}\left[e^{2\pi i\mu/3}h_{\mathrm{hop}}\right] \tag{S4}$$

which is 3 × 3 to be diagonalized. Here the real part of a matrix is defined by $\mathrm{Re}[X] = (X + X^{\dagger})/2$. More explicitly, equation (S4) is given by

$$\begin{pmatrix} \epsilon_r + 2t_{rr}\cos\tilde{k}_{z,\mu}a & -2it_{tr}\sin\tilde{k}_{z,\mu}a & -2it_{zr}\sin\tilde{k}_{z,\mu}a \\ 2it_{tr}\sin\tilde{k}_{z,\mu}a & \epsilon_t + 2t_{tt}\cos\tilde{k}_{z,\mu}a & 2t_{zt}\cos\tilde{k}_{z,\mu}a \\ 2it_{zr}\sin\tilde{k}_{z,\mu}a & 2t_{zt}\cos\tilde{k}_{z,\mu}a & \epsilon_z + 2t_{zz}\cos\tilde{k}_{z,\mu}a \end{pmatrix}, \tag{S5}$$

where $\tilde{k}_{z,\mu}a = k_z a + 2\pi\mu/3$. Since $|k_z a| \le \pi/3$, $\tilde{k}_{z,\mu}$ satisfies $|\tilde{k}_{z,\mu}a| \le \pi/a$. Now the physical meaning of $\tilde{k}_{z,\mu}$ is clear: a generalized Bloch momentum in a quasi-extended Brillouin zone. Ignoring the helical rotation, the three atoms in the unit cell are located periodically so that the Brillouin zone can be extended to a three times larger space. We call this a quasi-extended Brillouin zone since the helical rotation makes such a direct extension impossible. The cost of the extension is the introduction of off-diagonal hopping terms in equation (S5), which corresponds to a discretized version of the gauge potential.

Since exact diagonalization of equation (S5) is difficult, we treat $t_{\beta\alpha}$ perturbatively.

Perturbation theory gives the following eigenstates of equation (5).

$$|\widetilde{p_r}\rangle = |p_r\rangle + \frac{2it_{tr}\sin\tilde{k}_{z,\mu}a}{\epsilon_r - \epsilon_t}|p_t\rangle + \frac{2it_{zr}\sin\tilde{k}_{z,\mu}a}{\epsilon_r - \epsilon_z}|p_z\rangle, \tag{S6}$$

$$|\widetilde{p_t}\rangle = |p_t\rangle - \frac{2it_{tr}\sin\tilde{k}_{z,\mu}a}{\epsilon_t - \epsilon_r}|p_r\rangle + \frac{2t_{zt}\cos\tilde{k}_{z,\mu}a}{\epsilon_t - \epsilon_z}|p_z\rangle, \tag{S7}$$

$$|\widetilde{p_z}\rangle = |p_z\rangle - \frac{2it_{zr}\sin\tilde{k}_{z,\mu}a}{\epsilon_z - \epsilon_r}|p_r\rangle + \frac{2t_{zt}\cos\tilde{k}_{z,\mu}a}{\epsilon_z - \epsilon_t}|p_t\rangle. \tag{S8}$$

From the expressions equation (S3) and (S6)-(S8), the eigenstates of the full Hamiltonian [equation (S1)] are then given by

$$|\widetilde{p_r,\mu}\rangle = |\widetilde{p_r}\rangle \otimes |\mu\rangle, \tag{S9}$$

where $\otimes$ is the direct tensor product of the two spaces.

Note S2. Band characterization of the analytic eigenstates.

To match the eigenstates [equations (S6)-(S8)] with the results from the first-principles calculations (Supplementary Figure 3), we note that $|\widetilde{p_\alpha}\rangle$ is the perturbed eigenstate due to the hopping elements. Therefore, without hopping, *i.e.*, $\tilde{k}_{z,\mu} = 0$ gives the unperturbed eigenstates. Therefore, the orbital character at the zone center gives the characterization of each eigenstates. For instance, the top band in Supplementary Fig. 3b is $|\widetilde{p_z}\rangle$. Since $\tilde{k}_{z,\mu}$ is a momentum in a quasi-extended Brillouin zone, there are corresponding three bands in the first Brillouin zone. Therefore, it is natural to conclude that the top three bands correspond to $|\widetilde{p_z,\mu}\rangle$ for three μ values. Similarly, the three valence bands correspond to $|\widetilde{p_t,\mu}\rangle$. Our calculation for a wider energy range (not shown) shows that $|\widetilde{p_r,\mu}\rangle$ are located far below $|\widetilde{p_t,\mu}\rangle$.

Note S3. The relation between orbital angular momentum and injection current in a one-dimensional chiral Se chain.

According to Ref. 48 in main text, the photogalvanic current induced by a circularly-polarised light is given by

$$J = -\frac{4\pi e\tau}{\hbar}\int \frac{dk_z}{2\pi}[\Delta v_z(k_z)]\nu(k_z)\delta(\Delta\epsilon(k_z) - \hbar\omega), \tag{S10}$$

where τ is the relaxation time, $v_z(k_z)$ is the group velocity, ω is the frequency of the incident light, Δ means the difference between the initial and final states, and $\nu(k_z) = \left|P^{\mathrm{RCP}}(k_z)\right|^2 - \left|P^{\mathrm{LCP}}(k_z)\right|^2$ is the optical absorption efficiency difference for the right and left circular polarised lights. Using $\hbar v_z(k_z) = \partial_{k_z}\epsilon$, equation (S10) is converted to an energy integration.

$$J = -\frac{4\pi e\tau}{\hbar^2}\int \frac{d[\Delta\epsilon(k_z)]}{2\pi}\nu(k_z)\delta(\Delta\epsilon(k_z) - \hbar\omega) = -\frac{4\pi e\tau}{\hbar^2}\sum_{\Delta\epsilon(k_z) = \hbar\omega}\nu(k_z). \tag{S11}$$

When we consider a particular k_z value satisfying $\Delta\epsilon(k_z) = \hbar\omega$, we do not need to keep the summation.

To calculate $P^{\mathrm{RCP/LCP}}(k_z)$, it is necessary to calculate the matrix element of the perturbing electric field of the light. In Ref. 48, the system is periodic so that the velocity gauge was used, *i.e.*, $P^{\mathrm{RCP/LCP}} = \left(eA/m_e\right)\langle v|(p_x \pm ip_y)|c\rangle$, where A is the magnitude of the incident vector potential. However, for our case, the system is confined along the x and y direction so that the position gauge is more preferred, *i.e.*, $P^{\mathrm{RCP/LCP}} = eE\langle v|(x \pm iy)|c\rangle$ where E is the magnitude of the incident electric field. Then, one can show that $\nu = e^2E^2\mathrm{Im}[\langle I|x|F\rangle\langle F|y|I\rangle]$, where I and F are the initial and the final states, respectively. As a result, we obtain

$$J = -\frac{4\pi e\tau}{\hbar^2}e^2E^2\mathrm{Im}[\langle c|x|v\rangle\langle v|y|c\rangle], \tag{S12}$$

and if there are multiple k_z points satisfying $\Delta\epsilon(k_z) = \hbar\omega$, the contributions should be summed up. Combining equation (S12) and equation (5) gives equation (6) in the main text.

Note S4. Symmetry analysis of the emergence of nonzero orbital angular momentum components in bulk Se.

We consider a general three-dimensional system with time-reversal symmetry and a mirror symmetry with respect to the *zx* plane. First, the time-reversal symmetry implies that all the physical relations should be invariant under the transformation **k** → -**k** and **L** → -**L**. In other words,

$$\begin{aligned} L_x(k_x,k_y,k_z) &= -L_x(-k_x,-k_y,-k_z), \\ L_y(k_x,k_y,k_z) &= -L_y(-k_x,-k_y,-k_z), \\ L_z(k_x,k_y,k_z) &= -L_z(-k_x,-k_y,-k_z). \end{aligned} \tag{S13}$$

Similarly, the *zx* mirror symmetry implies that all the physical relations should be invariant under the transformation (k_x, k_y, k_z) → (k_x, -k_y, k_z) and (L_x, L_y, L_z) → (-L_x, L_y, -L_z). In other words,

$$\begin{aligned} L_x(k_x,k_y,k_z) &= -L_x(k_x,-k_y,k_z), \\ L_y(k_x,k_y,k_z) &= L_y(k_x,-k_y,k_z), \\ L_z(k_x,k_y,k_z) &= -L_z(k_x,-k_y,k_z). \end{aligned} \tag{S14}$$

Now we consider a more simplified case that the system is confined along the *x* and *y* directions. Then, k_x and k_y become meaningless. By the same argument as equations (S13)-(S14), dropping k_x and k_y, one obtains

$$\begin{aligned} L_x(k_z) &= -L_x(k_z), \\ L_y(k_z) &= L_y(k_z), \\ L_z(k_z) &= -L_z(k_z). \end{aligned} \tag{S15}$$

Therefore, $L_x(k_z) = L_z(k_z) = 0$ and only $L_y(k_z)$ can survive, which is depicted in Fig. 4b.

Note S5. Justification for the spin texture derived from the orbital texture.

When the total Hamiltonian is expressed as the sum of the orbital part (H_L), the spin part (H_S), and the spin-orbit coupling (SOC, $H_{L\text{-}S}$), *i.e.*, $H = H_L + H_S + H_{L\text{-}S}$, the inclusion of the SOC term necessitates the re-diagonalization of the Hamiltonian. However, it is important to note that our argument simplifies the situation under specific conditions: (i) when H_S is negligible, and (ii) when $H_{L\text{-}S}$ is not sufficiently large to favor the $J = L+S$ basis over the L-S basis. The validity of the first condition is supported by a separate DFT calculation conducted without the inclusion of SOC, which demonstrates the absence of a spin texture while confirming the presence of a distinct orbital texture. The second condition is fulfilled by two supportive results, the separate behaviors of the OAM and the SAM in Figure 2c and Figure 2d, and the well-separated orbital projection in Figure 1e.

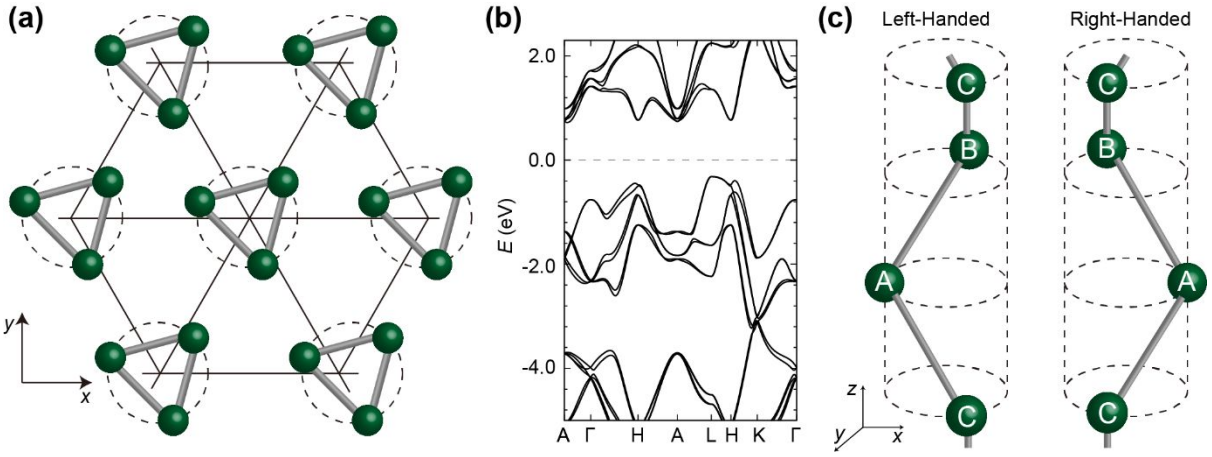

Figure S1. (a) Atomic and (b) electronic structure of bulk Se. (c) Schematic illustrations depicting the left-handed and right-handed crystal orientations.

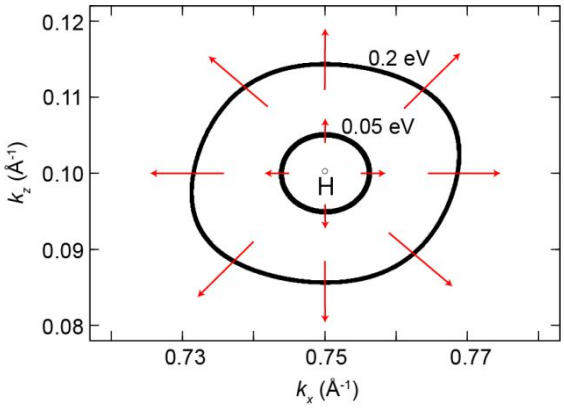

Figure S2. Orbital angular momentum profiles of the conduction band minimum at the H point in bulk Se without the inclusion of SOC. Black contour lines denote energy levels of 0.05 and 0.2 eV, respectively.

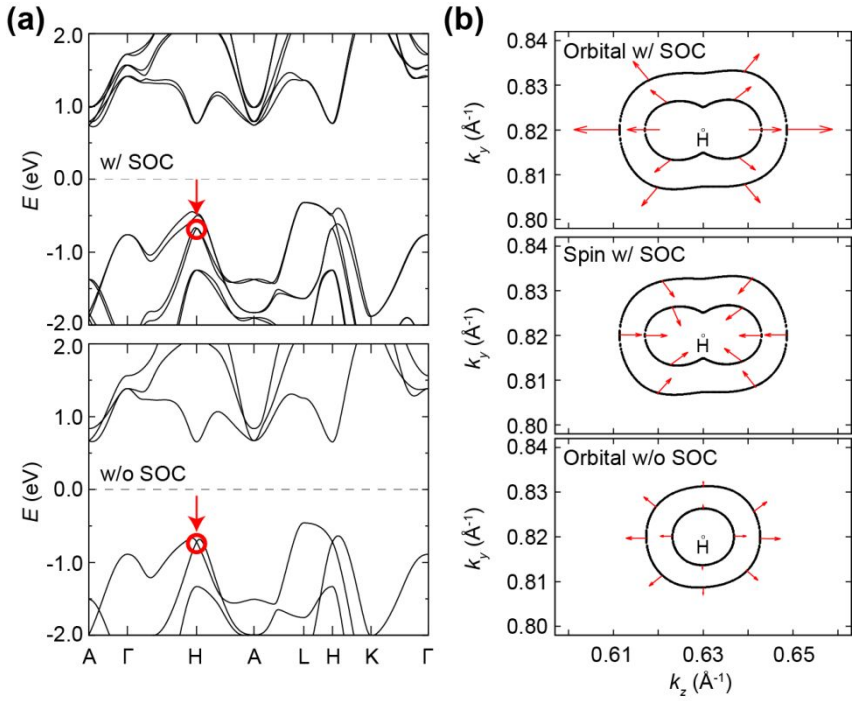

Figure S3. Orbital/Spin angular momentum of a helical Se chain at the H point in the valence band. (a) Calculated band structure of a Se chain with and without spin-orbit coupling (SOC). The red circles in (a) indicate the point where we analyze the orbital and spin angular momentum texture in (b). (b) Orbital and spin angular momentum profiles of the valence band at the H point in bulk Se in the presence or absence of SOC.

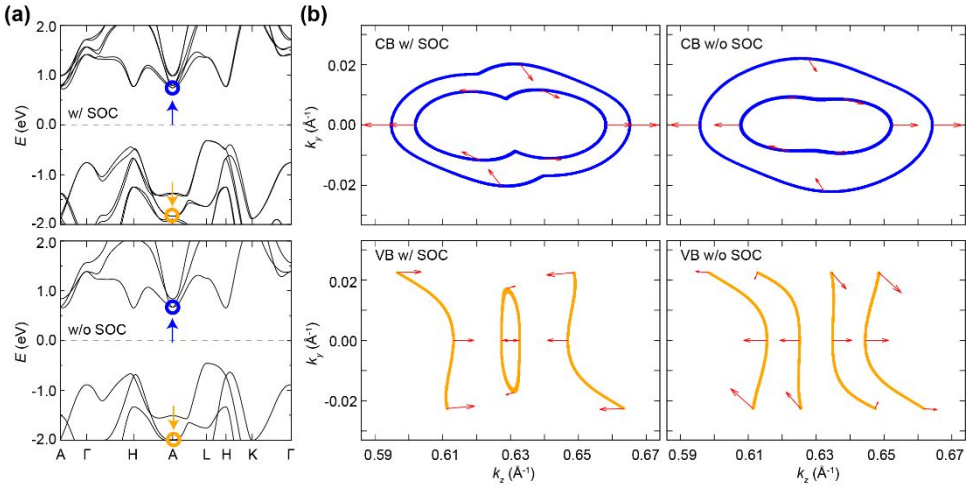

Figure S4. Orbital/Spin angular momentum of a helical Se chain around the A point. (a) Calculated band structure of a Se chain in the presence or absence of SOC. The orange (blue) circle in (a) indicate the valence (conduction) band point where we investigate the orbital and spin angular momentum texture in (b). (b) Orbital angular momentum profiles of the valence (orange) and conduction (blue) bands at the A point in bulk Se in the presence or absence of SOC.

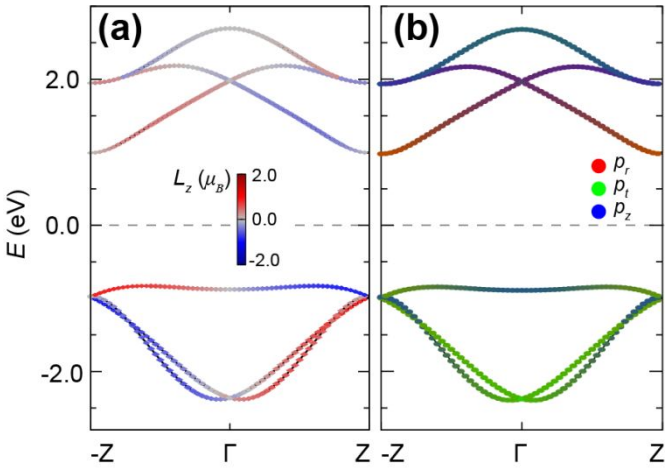

Figure S5. Calculated band structure of a Se chain with (a) orbital-angular-momentum resolution (L_z), and (b) atomic-orbital resolution using radial (p_r), tangential (p_t), and axial (p_z) *p*-orbitals as the orbital bases.

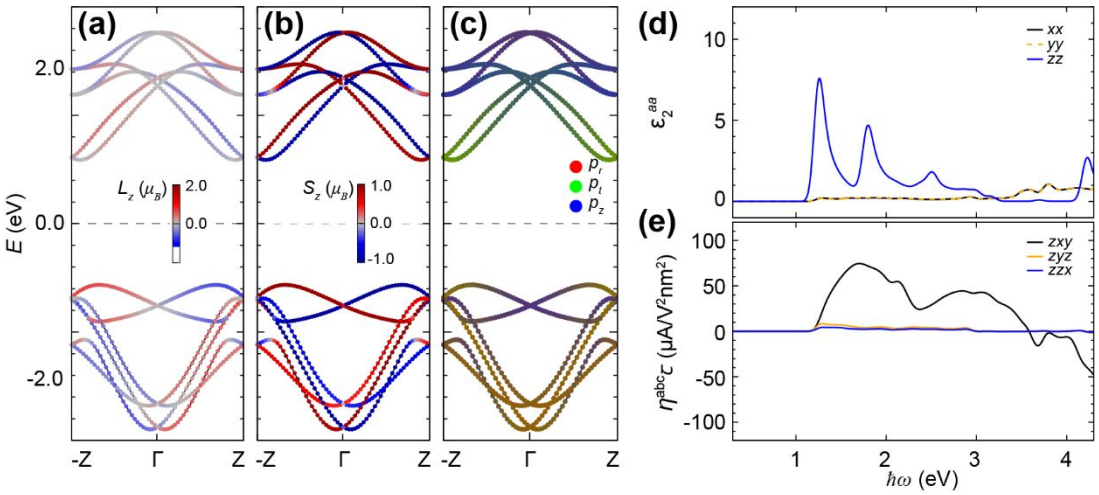

Figure S6. Calculated band structure of the Te chain with (a) orbital-angular-momentum resolution (L_z), (b) spin-angular-momentum resolution (S_z), and (c) atomic-orbital resolution using radial (p_r), tangential (p_t), and axial (p_z) p-orbitals as the orbital bases. (d) Diagonal components of the imaginary parts of the dielectric tensor of helical Te chain. (e) Calculated circular photogalvanic current (injection current) spectrum of the Te chain as a function of the frequency of a circularly polarized light.

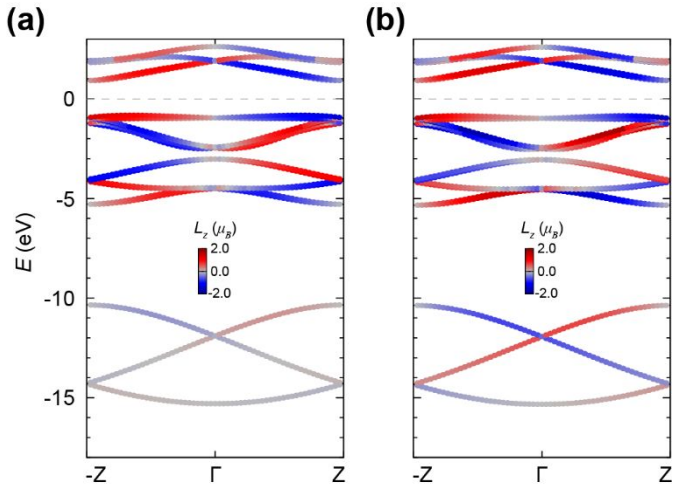

Figure S7. Calculated band structure of a Se chain with orbital-angular-momentum resolution (L_z) using the method of (a) atomic orbital decomposition and (b) $\mathbf{r} \times \mathbf{p}$ operation.

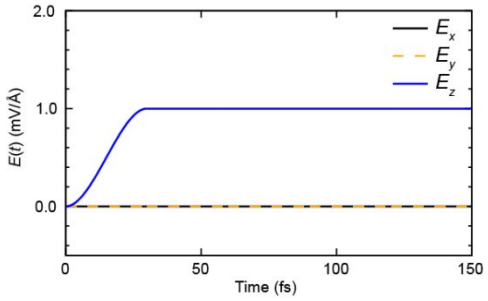

Figure S8. Time profile of the electric field used in the calculation of current-induced magnetism (Figure 2)

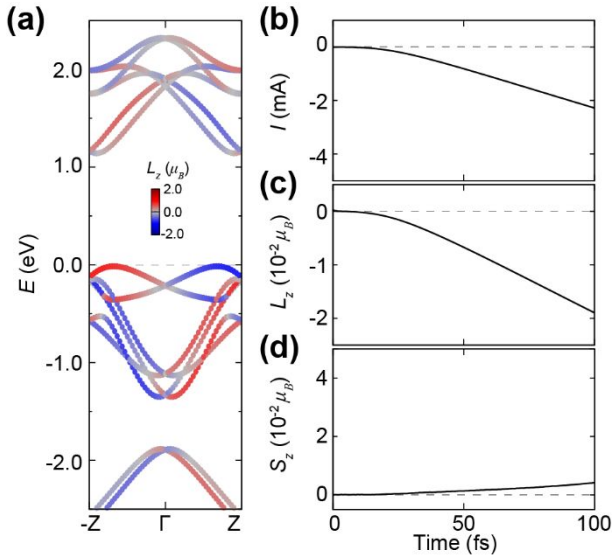

Figure S9. (a) Calculated band structure of a Te chain with orbital-angular-momentum resolution (L_z) under hole doping (0.1 *e*/unit) in the presence of SOC. Calculated (b) induced current (I), (c) total orbital angular momentum (L_z), and (d) total spin angular momentum (S_z) induced by a dc field (10^{-3} V/Å) along the Te chain. The quantitative definitions of I, L_z, and S_z are described in the Methods section.

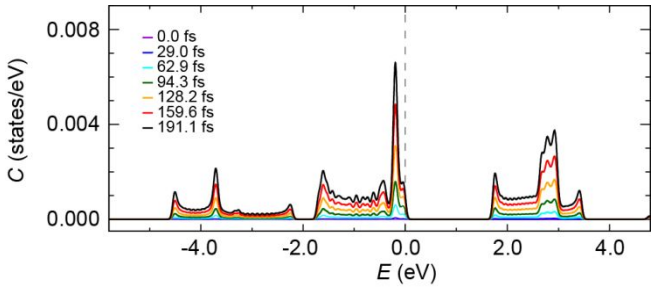

Figure S10. Time evolution of the density of states projected onto the unperturbed electron/hole states in a Se chain under a 0.0001 V/Å field.

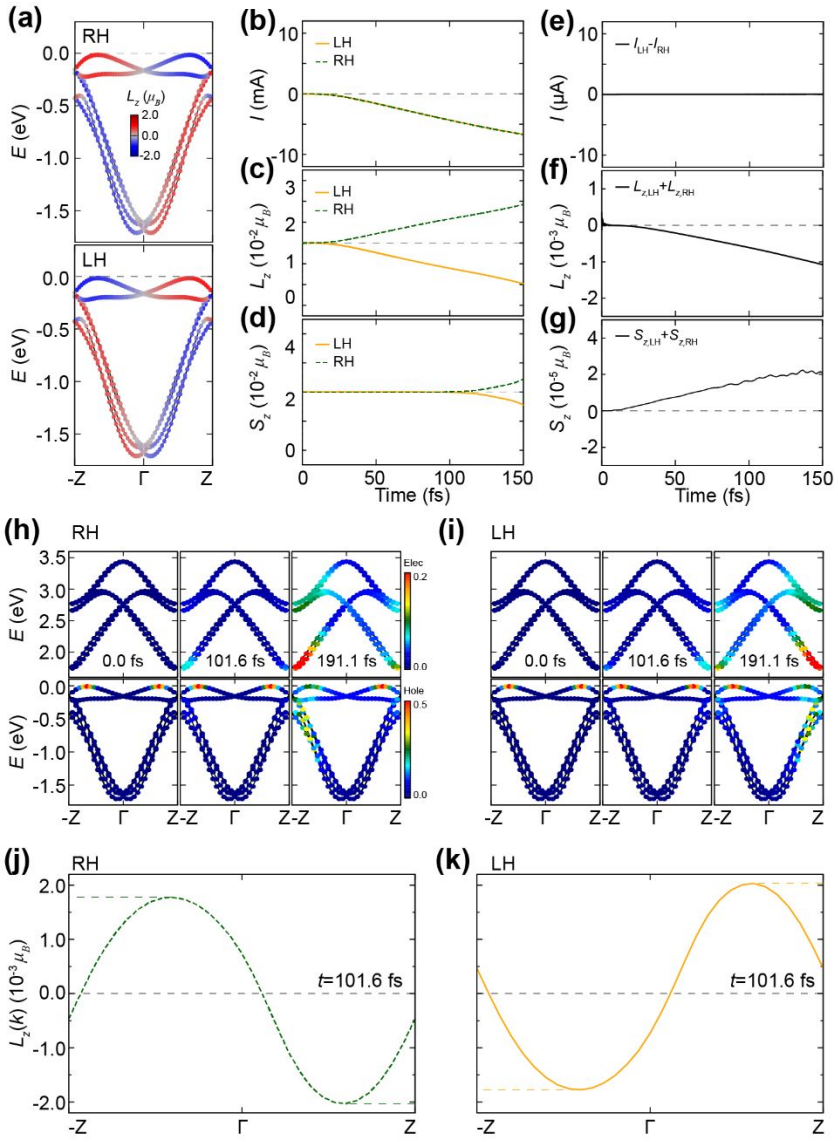

Figure S11. Chirality-dependent current-induced magnetism in a helical Se chain. (a) Calculated band structure of a right-handed (RH) or left-handed (LH) Se chain with orbital-angular-momentum resolution (L_z) under hole doping (0.1 *e*/unit). Calculated (b) induced current (I), (c) total orbital angular momentum (L_z), and (d) total spin angular momentum (S_z) induced by a dc field (10^{-3} V/Å) along the Se chain for RH and LH chains. (e) Difference in induced current (I) between RH and LH chains. Summation of LH and RH results for (f) total orbital angular momentum (L_z) and (g) total spin angular momentum (S_z). Time evolution of the electron/hole weights projected onto the ground-state band structure of the (h) right-handed and (i) left-handed Se chain with +z-direction E-field. Calculated momentum-resolved orbital angular momentum in the (j) RH and (k) LH Se chain at t=101.6 fs.

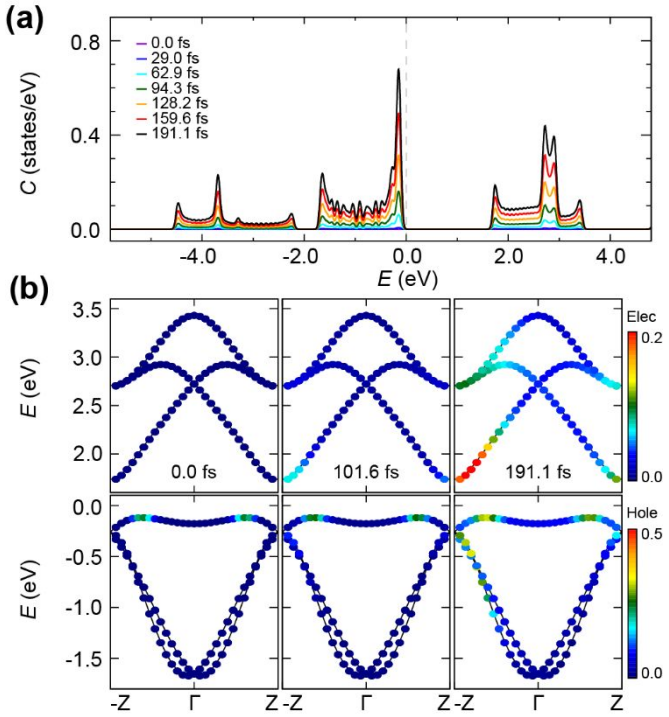

Figure S12. (a) Time evolution of the density of states projected onto the unperturbed electron/hole states in a Se chain without the inclusion of SOC. (b) Time evolution of the electron/hole weights projected onto the ground-state band structure of the Se chain without the inclusion of SOC.

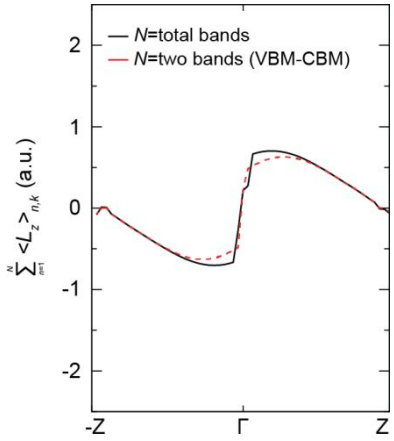

Figure S13. Comparison of total orbital angular momentum and two-band approximated orbital angular momentum.

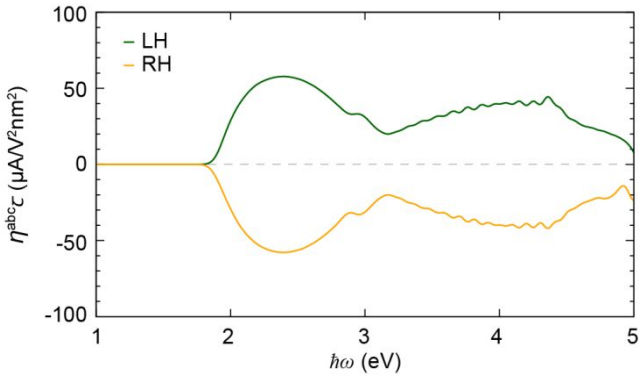

Figure S14. Handedness dependence of calculated circular photogalvanic current (injection current) spectrum of a Se chain as a function of the frequency.

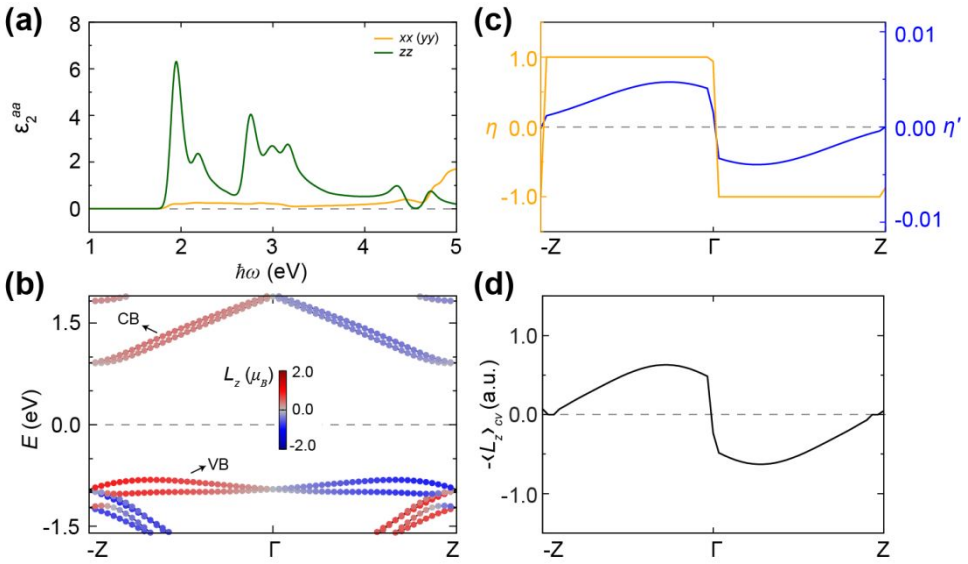

Figure S15. Linear absorption spectrum and circular dichroism for the band-edge transition. (a) Diagonal components of the imaginary parts of the dielectric tensor of a helical Se chain. (b) Calculated band structure of the Se chain with orbital-angular-momentum resolution (L_z) near Fermi level. Two bands, denoted as CB and VB, have been selected to examine the relationship between circular dichroism and orbital angular momentum in the Se chain. (c) Circular dichroism (η) and its denominator (η') for the band-edge transition in the Se chain. We define two different circular dichroisms for the band-edge transition $\eta(\mathbf{k}) = \frac{|P_+^{cv}(\mathbf{k})|^2 - |P_-^{cv}(\mathbf{k})|^2}{|P_+^{cv}(\mathbf{k})|^2 + |P_-^{cv}(\mathbf{k})|^2}$ and $\eta'(\mathbf{k}) = |P_+^{cv}(\mathbf{k})|^2 - |P_-^{cv}(\mathbf{k})|^2$, where $P_\pm^{cv}(\mathbf{k}) = \frac{1}{\sqrt{2}}[P_x^{cv}(\mathbf{k}) \pm iP_y^{cv}(\mathbf{k})]$ and $\mathbf{P}^{cv} = \langle \psi_{c,\mathbf{k}} | \hat{\mathbf{p}} | \psi_{v,\mathbf{k}} \rangle$. c and v indicate conduction and valence bands, respectively. (d) Calculated two-band orbital angular momentum ($\langle L_z \rangle_{cv}$) between the CB and the VB in the Se chain.

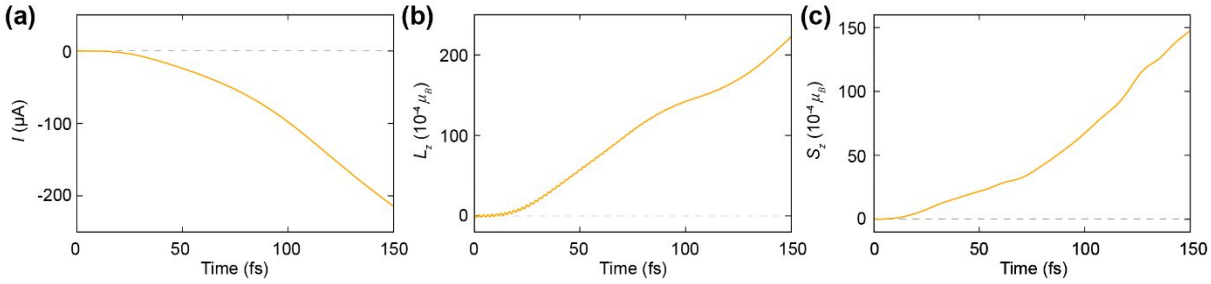

Figure S16. Calculated (a) induced current (I), (b) total orbital angular momentum (L_z), and (c) total spin angular momentum (S_z) induced by a circularly polarized light with intensity of 0.51 V/Å and frequency of $\hbar\omega$=2.02 eV as a function of time.

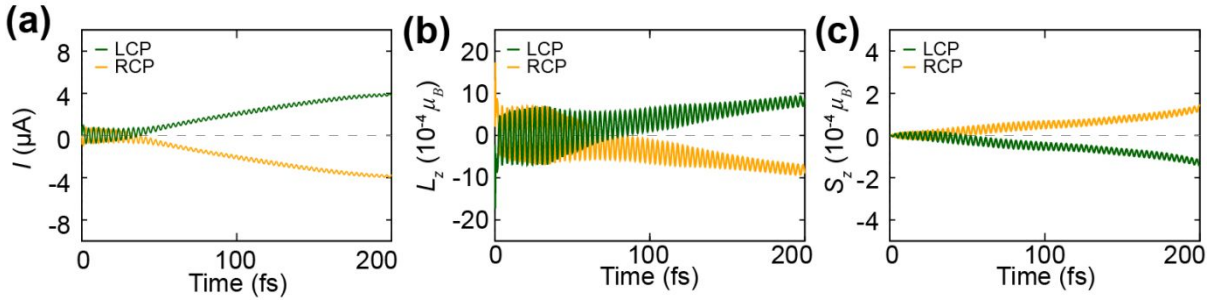

Figure S17. Calculated (a) induced current (I), (b) total orbital angular momentum (L_z), and (c) total spin angular momentum (S_z) induced by circularly polarized lights with intensity of 0.051 V/Å and frequency of $\hbar\omega$=1.7 eV as a function of time.

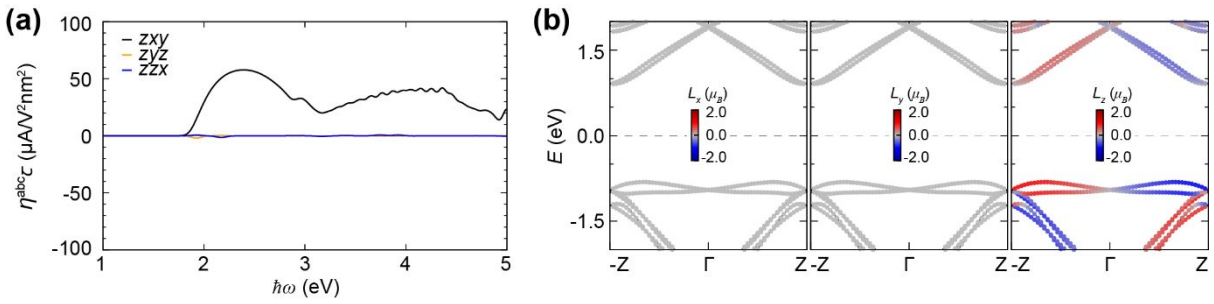

Figure S18. (a) Calculated circular photogalvanic current (injection current) spectrum of a Se chain as a function of the frequency for various circularly polarized lights. (b) Calculated band structure of the Se chain with orbital-angular-momentum resolution (L_x, L_y, and L_z).

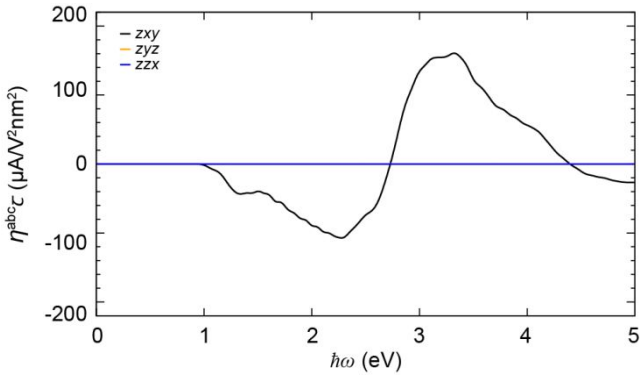

Figure S19. Calculated circular photogalvanic current (injection current) spectrum of bulk Se as a function of the frequency.

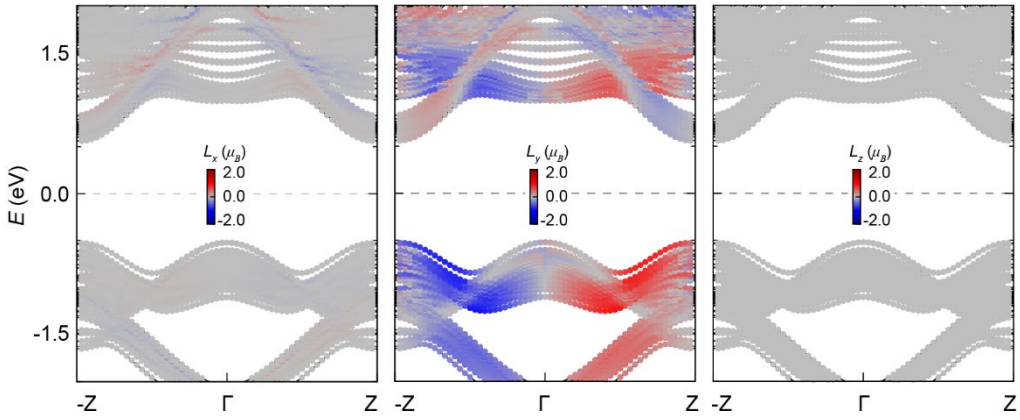

Figure S20. Calculated band structure of the domain boundary between LH and RH domains with orbital-angular-momentum resolution (L_x, L_y, and L_z).

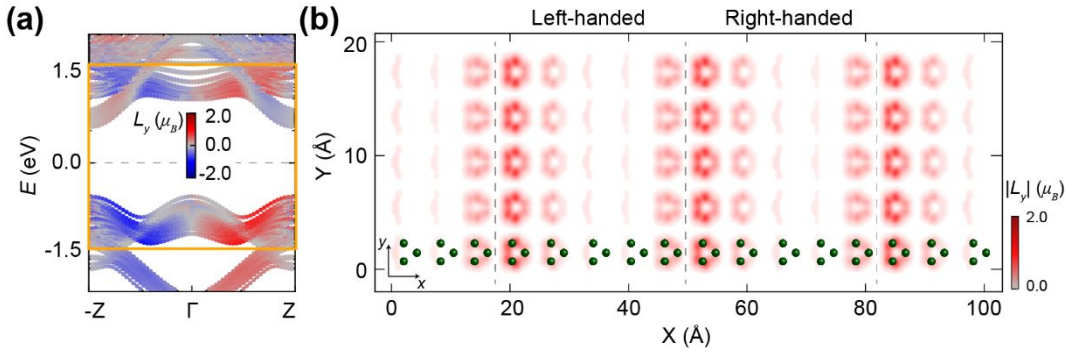

Figure S21. (a) Calculated band structure of the domain boundary between the left-handed and right-handed Se domains with orbital-angular-momentum resolution (L_y). (b) Real space representation of the states with a non-zero L_y component inside the orange box in (a). Grey dotted lines indicate the boundary between the left-handed and right-handed Se chains.

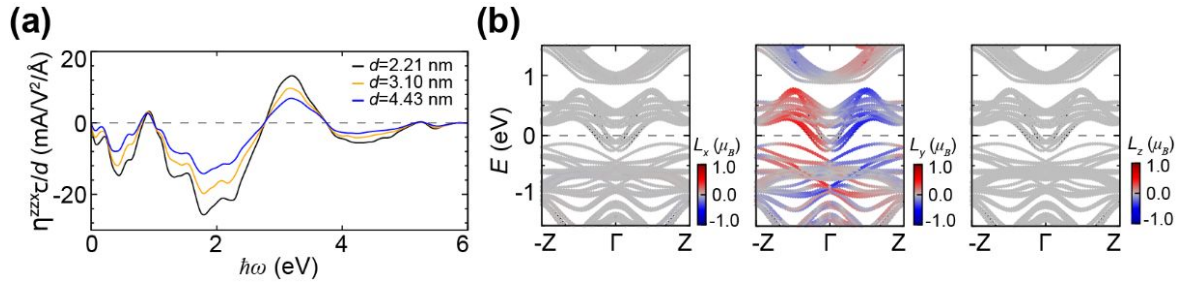

Figure S22. (a) Variation in the injection current spectrum per unit length of the domain structure upon the domain length (*d*) of helical Te chain. (b) Calculated band structure of the alternating chains with orbital-angular-momentum resolution of helical Te chain.

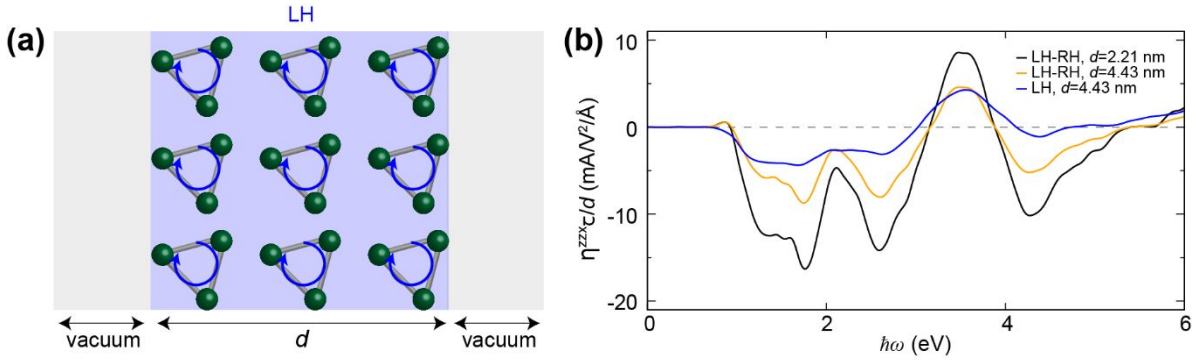

Figure S23. (a) Schematic drawing of a slab structure for left-handed (LH) or right-handed (RH) chains exposed to vacuum. (b) Calculated injection current spectrum per unit length for the LH slab and the LH-RH domain structures with respect to domain length (*d*).